Aerosol Dynamic Processes of Soot Aggregates in a Laminar Ethene Diffusion Flame

R. PURI, T. F. RICHARDSON, and R. J. SANTORO
Department of Mechanical Engineering, Pennsylvania State University, University Park, PA 16802

R. A. DOBBINS
Division of Engineering, Brown University, Providence, RI 02912

Laser scattering/extinction tests on a coannular ethene diffusion flame were analyzed using cross sections for polydisperse aggregates. Using an improved experimental arrangement that allowed simultaneous measurement of light scattering at multiple angles, it was possible to determine the fractal dimension of the aggregates in the flame. The analysis also yields the mean-square radius of gyration, the aggregate number concentration, the average number of primary particles per aggregate, as well as the volume average of the volume-mean diameter as a function of height or residence time along the particle path of maximum soot concentration in this flame. These results lead to the conclusion that soot aerosol dynamic processes in the laminar ethene flame are partitioned into four regions. Low in the diffusion flame there is a region of particle inception that establishes the number of primary particles per unit volume that remains constant along a prescribed soot pathline. In the second region, there is sustained particle growth through the combined action of cluster-cluster aggregation (CCA) accompanied by heterogeneous reactions contributing to monomer-cluster growth. Oxidation processes occur in the third region where CCA continues. If aggregate burnout is not complete in the oxidation region, then smoke is released to the surroundings in the fourth region where reactions cease but clusters continue to grow by CCA. The experiments yield the CCA growth rate within the flame which compares favorably with the theoretical value. The similarities and differences between this data reduction and the traditional analysis based on the use of cross sections for Rayleigh spheres and Mie theory spheres is discussed.

NOMENCLATURE

a_{ij}	function defined in Table 1
b_{ij}	function defined in Table 1
c_{ij}	function defined in Table 1
c_m	mass of particles per unit volume
c_p	function defined in Table 1
$\overline{C_{vv}(\theta)}$	mean aggregate scattering cross section for a population of polydisperse aggregates, averaged over all orientations, when both incident light and scattered light are perpendicular to the plane of observation
D	diameter of a spherical particle
D_{30}	volume weighted average of the volume equivalent diameters of a population of aggregates
D_f	fractal dimension
d_{ij}	function defined in Table 1
d_p	diameter of the primary particles
d_{po}	diameter of the primary particles as determined by optical observations
d_{pt}	diameter of the primary particles as determined by TEM observations
e	2.718
$E(m)$	function of m defined by Eq. 14
$f(x)$	function defined by Eqs. 7 and 8
$F(m)$	function of m defined by Eq. 2
f	the specific surface growth or oxidation rate of the primary particles defined by Eq. 23
f_n	the ratio $\overline{n^2}/(\overline{n^1})^2$
f_v	volume of particles per unit volume
$g(k^2\overline{R_g^2})$	the function defined by Eq. 16
$\overline{I^A(\theta_i)}$	normalized cross section for vv differential scattering by a polydisperse aggregate population in random orientation
I_0	power of the incident laser beam

0010-2180/93/$5.00

Copyright © 1993 by The Combustion Institute
Published by Elsevier Science Publishing Co., Inc.

k wave number equal to $2\pi/\lambda$
k_B Boltzmann constant
k_f prefactor in the fractal power law, in Eq. A1
K_a cluster–cluster aggregation rate
K_{abs} absorption coefficient of the aggregate population
K_{ext} extinction coefficient of the aggregate population
L_{mx} maximum dimension of an aggregate
m complex refractive index
n number of primary particles per aggregate
n_0 minimum value of n for a population of polydisperse aggregates
n_g geometric mean of n for a population of polydisperse aggregates
n_∞ maximum value of n for a population of polydisperse aggregates
$\overline{n^q}$ qth moment of the size probability function for a population of polydisperse aggregates
$p(n)$ size distribution function for a population of polydisperse aggregates
N_a number of aggregates per unit volume
N_p number of primary particles per unit volume
q_i $2k \sin(\theta_i/2)$, modulus of the scattering vector
$Q_{vv}(\theta_i)$ measured cross section for vv scattering per unit volume
r_{ij} the function defined in Table 1
R_g radius of gyration of an aggregate equal to the square root of the mean square distances from the center of mass of the aggregate to center of each primary particle
$\overline{R_g^2}$ mean-square radius of gyration for a population of polydisperse aggregates as defined by Eq. 6
R_{ij} ratio of $Q_{vv}(\theta_i)/Q_{vv}(\theta_j)$
s_0 normalization constant in Eq. A5
S_t surface area of aggregates per unit volume
t time
T temperature
v particle volume
z vertical distance measured from the mouth of the burner
x_i $q_i^2\overline{R_g^2}$
x_p $\pi d_p/\lambda$

Greek Symbols

λ wavelength of light
θ_i, θ_j scattering angles measured from the direction of propagation of the incident light
$\bar{\kappa}$ function of D_f, k_f, and $p(n)$ defined by Eq. A3
ω_p ratio of total scattering cross section to extinction cross section for primary particles
ρ_p density of the primary particle material
ρ_{sa} ratio of total scattering cross section to absorption cross section for a population of polydisperse aggregates
σ_g geometric standard deviation used in Eq. A5

INTRODUCTION

In a related earlier paper, the use of the optical cross sections for polydisperse aggregates was described to reduce the data from laser scattering/extinction tests conducted on the soot formed in a laminar diffusion flame using ethene as the fuel [1]. This development resulted from the recognition that the soot particles outside the inception region in the laminar ethene flame are found in the form of clusters of primary particles that possess a fractal-like character [2, 3]. These ideas, which were recognized in part in the earlier carbon black literature, have been formalized through the use of optical properties of mass fractals [4–6]. The optical cross sections for polydisperse aggregates composed of an absorbing material were subsequently formulated [7]. The present work takes advantage of an improved experimental arrangement wherein the intensity of the scattered laser light was measured simultaneously at three angles θ_i—45°, 90°, and 135°. Line-of-sight extinction measure-

ments were obtained separately from the simultaneous angular scattering measurements and reduced to point measurements by a tomographic inversion procedure [8].

The simultaneous observation of the angular distribution of scattered light results in an improved data set over that obtained by the sequential data acquisition approach previously used [1]. Using the present approach, ratios of the scattered light measurements at various angles are less affected by small variations due to changes in the flame conditions (e.g., flame movement) since angular dissymmetry information is constructed from data taken simultaneously at each angle. Using these improved data, a more detailed analysis of the optical observations is described herein. This approach allows an iterative analysis to determine the fractal dimension rather than imposing a value for this quantity based on work by other investigators, as was done previously [1]. Additionally, new information of the prefactor, k_f, in the fractal power law analysis has been incorporated into the present work. These developments allow new information to be derived on the surface growth and oxidation rates observed in these flames and to further refine the treatment of the aggregation process. A clearer relationship between the number of aggregates per unit volume and the number of primary particles per unit volume is also observed. From these observations we arrive at a global description of physical processes associated with the formation, growth, and oxidation of the soot aggregates formed in a laminar ethene diffusion flame.

The data reduction performed herein is based on the optical cross sections that have been formulated for polydisperse aggregates that apply over a wide range of size parameters, widths of distribution functions, and refractive indices for absorbing or dielectric particles [7]. The differential and total scattering cross sections are a generalization of the numerical simulations of aggregates formed by Langevin mechanics [9]. The aggregates found in the latter study comply with the power law for mass fractals even when the number of primary particles per aggregate are as small as $O(10)$. Such aggregates are too small to display the scale similarity property of mass fractals, and they are said to be "fractal-like." Optical absorption cross sections of aggregates were based on the results of various investigators who have found them to be well approximated by the volume absorption of the component primary particles.

EXPERIMENTAL APPARATUS AND DATA ACQUISITION

The coannular burner used in these experiments consists of an inner tube of 11.1 mm i.d., which is supplied with c.p. grade ethene at a flow rate of 3.85 cm^3/s. A coannular air stream is provided through a ceramic honeycomb grid filling the intervening air region which has a 101.6 mm i.d. The air stream flow rate is 713 cm^3/s and is guided by a metal chimney with slots that permit the passage of a laser beam and the observation of the light scattering that it produces. A detailed description of this coannular burner is given elsewhere [10]. With ethene as a fuel, the resulting flame height is about 88 mm, and the soot formed within the flame is fully oxidized within the flame.

The apparatus used to measure the laser extinction and scattering signals from soot particles in the flame utilized a 4-W argon ion laser operating at the 514.5-nm laser line. The incidence power, I_0, was 0.5 W and was modulated using a mechanical chopper operating at 1015 Hz. The incident beam was passed through a polarization rotator that allowed adjustment of the polarization orientation. For these experiments all measurements were obtained for vertically polarized light having a polarization ratio of better than 400 : 1.

The beam was focused into the burner region with a 400-mm focal length lens, which resulted in a beam whose diameter was approximately 0.2 mm. The transmitted power, I, was measured using a silicon photodiode after attenuation by neutral density filters (N.D. $\approx$ 2.0) to reduce the beam intensity to acceptable levels. Scattered light receivers were located at angles 45°, 90°, and 135° with respect to the forward propagation direction of the incident beam. Each of the scattered light receivers consisted of a polarizer, circular aperture, collection lens, pinhole aperture, laser line filter

for 514.5 nm ($\Delta\lambda$ = 1 nm) and a Hammamatsu R928 photomultiplier tube. A circular aperture (12.7 mm diameter) defined the scattered light collection solid angle to be 1.2×10^{-3} sr. A pinhole aperture (1 mm diameter) defined the length of the sample volume to be 1 mm since the optical system was set up to have unity magnification. The polarizers had rejection ratios of 1×10^{-4}.

Each of the scattered light detectors was connected to a lock-in amplifier that was operated with a time constant of 0.30 s. Data acquisition from the lock-in amplifiers using an IBM-XT personal computer employing a GPIB interface provided for near-simultaneous data acquisition from each detector. Consequently, the resulting dissymmetry measurements formed from the ratio of the detector signals were not subject to problems resulting from small changes in the probe volume location due to flame movement over the period of the measurement. The time between acquisition of sequential measurements from the individual lock-in amplifiers was determined to be less than 100 μs. This procedure resulted in improved angular dissymmetry measurements as compared with previously reported results [1]. Separate runs were used to measure the dissymmetry ratio and the extinction measurements since only three lock-in amplifiers were available. However, previous work has shown that the present laminar diffusion flame apparatus produced highly reproducible measurement conditions.

The scattered light detection systems were calibrated using a Rayleigh scattering technique previously described [10]. This approach accounts for the effects of the incident laser power, sample volume, light collection efficiency, photomultiplier sensitivity, and electronic gain of the system.

Radial profiles of light scattering and extinction measurements were obtained at fixed axial locations in the flame (Z = 10, 15, 20, 30, 50, 60, and 70 mm). The local soot extinction (and subsequently, the soot volume fraction) were obtained from the extinction measurements using a tomographic inversion procedure [8], while the ratio of the scattered light signals, R_{ij}, was calculated directly after accounting for the detection system calibrations. The data analysis was carried out for soot aggregates that were formed along the particle path possessing the maximum soot volume fraction.

The information on the particle path, which is needed to relate the measurements made at different flame locations, was achieved using measurements of the velocity field in the flame. These velocity measurements were obtained using a single component laser velocimeter. Sequential profiles were obtained to provide information on both the radial and axial components of the velocity field. These measurements were then used to construct the appropriate particle path possessing the maximum soot volume fraction in the flame [11].

DATA ANALYSIS

The data analysis uses the cross sections [7] that were previously employed [1] in a more advantageous procedure that no longer requires an assumed value of the fractal dimension D_f because of the improved quality of the angular scattering data as discussed previously. The normalized cross section for vv differential scattering (i.e., vertically polarized scattered light produced by vertically polarized incident light) by a polydisperse aggregate population in random orientation is defined by

$$\overline{I^A(\theta_i)} = \frac{k^2 \overline{C_{vv}(\theta_i)}}{x_p^6 F(m)}, \tag{1}$$

where $\overline{C_{vv}(\theta_i)}$ is the population-averaged differential scattering cross section, k is the wavenumber equal to $2\pi/\lambda$, where λ is the wavelength of light, and x_p is $\pi d_p/\lambda$, where d_p is the diameter of the primary particles. The volumetric scattering cross section, $Q_{vv}(\theta_i)$, cm^{-1} sr^{-1}, which is directly measured through a calibration procedure described elsewhere [10], is the product of the scattering cross section $\overline{C_{vv}(\theta_i)}$ (cm^2), and the aggregate number concentration N_a (cm^{-3}). The quantity $F(m)$ is given by

$$F(m) = \left| \frac{m^2 - 1}{m^2 + 2} \right|^2, \tag{2}$$

where m is the complex refractive index of the soot particulate material. Several moments of

the aggregate probability distribution function (pdf) enter into the relations for the optical cross sections. The qth moment of the pdf is defined by

$$\overline{n^q} = \sum_n n^q p(n). \tag{3}$$

Here the discrete function $p(n)$ is defined such that $\Sigma p(n)$ over the interval n_1 to n_2 represents the fraction of the population having more than n_1 and less than n_2 primary particles per aggregate. The first moment $\overline{n^1}$ is the average number of primary particles per aggregate. The moment ratio f_n is defined by

$$f_n = \overline{n^2}/\left(\overline{n^1}\right)^2 \tag{4}$$

and can be used to relate $\overline{n^2}$ to $\overline{n^1}$. While limited information is available on $p(n)$, reasonable estimates of moment ratios such as f_n can be made as discussed in the Appendix. Each aggregate has a volume-equivalent diameter $D = n^{1/3} d_p$, and the volume-weighted average diameter of the volume-equivalent spheres, $D_{30} = (\overline{n^1})^{1/3} d_p$, is an important quantity that appears in the equations given below [3].

The quantity $\overline{I^A(\theta)}$ divided by $\overline{n^2}$ is a function only of the quantity $x_i = q_i^2 \overline{R_g^2}$, where q_i, the modulus of the scattering vector, is given by

$$q_i = 2k \sin(\theta_i/2), \tag{5}$$

and the mean-square radius of gyration is defined by

$$\overline{R_g^2} = \frac{\sum_n R_g^2(n) n^2 p(n)}{\sum_n n^2 p(n)}. \tag{6}$$

Thus for $0 < x_i < 1.5D_f$ where D_f is the fractal dimension, $f(x_i)$ is given by the Guinier law

$$\frac{\overline{I^A(\theta_i)}}{\overline{n^2}} = f(x_i) = \exp(-x_i/3). \tag{7}$$

This expression was originally presented as an approximate relationship for scattering of x-rays by an electron cloud, and is also applicable to aggregates [5]. Recently Eq. 7 has been found to provide a good description of differential scattering for populations of polydisperse aggregates irrespective of the width of distribution function [7] when the mean-square radius of gyration defined by Eq. 6 is employed.

For $x_i \ll 1$, $f(x_i) \to 1$ and the differential scattering cross sections of an aggregate is the same as for a sphere of equal volume. To a good approximation in this instance both the vv scattering cross section and the absorption cross section depend only upon the volume of the material irrespective of the particle shape. Thus a small sphere and a small aggregate of equal volume behave identically in both vv scattering and extinction, and observations of these cross sections provide no information on which of these two disparate morphologies is actually present. For most of the observations reported below, the aggregates were large enough so that $x_i \approx 1$ or larger.

When $x_i > 1.5D_f$, the power law form for $f(x_i)$ is applicable:

$$f(x_i) = \left(\frac{1.5D_f}{ex_i}\right)^{D_f/2}, \tag{8}$$

where $e = 2.718$.

For two angles with x_i and x_j both $\leq 1.5D_f$, it follows that the measured cross sections at two angles can be used to determine the mean-square radius of gyration without a knowledge of refractive index or any information on the size distribution function. From Eqs. 1 and 7 we find

$$\overline{R_g^2} = \frac{a_{ij}}{k^2} \ln(R_{ij}), \tag{9}$$

where $R_{ij} = Q_{vv}(\theta_i)/Q_{vv}(\theta_j)$ and a_{ij} is a constant (Table 1) for given angles and $1 < R_{ij} \leq$

TABLE 1

Equations for the Constants Used in Determination of the Mean-Square Radius of Gyration Using Eqs. 9 or 10.

$r_{ij} = \sin(\theta_i/2)/\sin(\theta_j/2)$	$a_{ij} = 0.75 \Big/ \left[\sin^2\left(\frac{\theta_j}{2}\right) - \sin^2\left(\frac{\theta_i}{2}\right)\right]$
$b_{ij} = \exp[0.5\, D_f(1 - r_{ij}^2)]$	$c_{ij} = (r_{ij})^{-D_f}$
$d_{ij} = c_{ij}/C_p$	$C_p = (1.5\, D_f/e)^{D_f/2}$

b_{ij}. When $\theta_j(\theta_j > \theta_i)$ is such that $q_j^2\overline{R_g^2}$ is greater than $1.5D_f$ (corresponding to $b_{ij} < R_{ij} < c_{ij}$), both Eqs. 7 and 8 must be employed and a transcendental equation for x_i results:

$$x_i \exp\left(\frac{-x_i}{1.5D_f}\right) = \left(\frac{R_{ij}}{d_{ij}}\right)^{2/D_f}. \tag{10}$$

The equations for the quantities a_{ij}, b_{ij}, c_{ij}, and d_{ij}, which are given in Table 1, depend upon the angles selected and, with one exception (a_{ij}), also depend upon D_f. From Eq. 8 it follows that the slope of the curve of log $(\overline{I^4}/\overline{n^2})$ versus log x_i is equal to $-D_f/2$. This property has been widely used to infer the fractal dimension of populations of aggregate structures (e.g., Ref. 4).

The extinction coefficient for a polydisperse population of aggregates is the sum of the absorption coefficient and the total scattering coefficient [7]; also see Appendix II of Ref. 1. It can be expressed as

$$K_{ext} = K_{abs}(1.0 + \rho_{sa}), \tag{11}$$

where K_{abs} is given by

$$K_{abs} = \frac{4\pi N_a \overline{n^1} x_p^3 E(m)}{k^2}, \tag{12}$$

and ρ_{sa}, the ratio of scattering to absorption, is given by

$$\rho_{sa} = \omega_p f_n \overline{n^1} g\left(k^2\overline{R_g^2}\right) \tag{13}$$

and $E(m)$ is given by

$$E(m) = -\mathrm{Im}\left(\frac{m^2 - 1}{m^2 + 2}\right). \tag{14}$$

Here ω_p is the albedo of the primary particle and is given by

$$\omega_p = \frac{2}{3}x_p^3 \frac{F(m)}{E(m)} \tag{15}$$

and

$$g\left(k^2\overline{R_g^2}\right) = \left(1 + \frac{4}{3D_f}k^2\overline{R_g^2}\right)^{-D_f/2}. \tag{16}$$

The functions of $f(x_i)$ and $g(k^2\overline{R_g^2})$ determine the departure of the scattering cross sections from the Rayleigh values that are applicable for small aggregates. The soot volume fraction is related to the aggregate average volume and number concentration by

$$f_v = \frac{\pi d_p^3 \overline{n^1} N_a}{6}, \tag{17}$$

and, in view of the Eq. 12 for the volumetric absorption, the volume fraction can be expressed as

$$f_v = \frac{K_{abs}}{3kE(m)}. \tag{18}$$

The volumetric vv scattering cross section is the product of the corresponding mean cross section and the aggregate number concentration N_a and is given by

$$Q_{vv}(\theta_i) = \frac{f_n\left(\overline{n^1}\right)^2 x_p^6 F(m) N_a f(x_i)}{k^2}. \tag{19}$$

Specifying $\theta_2 = 90°$ in the above expression, dividing by K_{abs}, and noting that $\overline{n^1}d_p^3 = D_{30}^3$, we find

$$D_{30} = \left(\frac{\lambda}{\pi}\right)\left(\frac{4\pi E(m) Q_{vv}(\theta_2)}{f_n F(m) f(x_2) K_{abs}}\right)^{1/3}. \tag{20}$$

The aggregate number concentration N_a is given by

$$N_a = \frac{f_v}{\frac{\pi}{6}D_{30}^3}. \tag{21}$$

The fractal power law for polydisperse aggregates that is discussed further in the Appendix leads to [3]

$$d_{po} = \frac{D_{30}^3}{\bar{\kappa}\overline{R_g^2}}. \tag{22}$$

From Eqs. 20 and 22 it is apparent that d_{po} is inversely proportional to the quantity $[\bar{\kappa} f_n F(m)/E(m)]$ and is clearly sensitive to

both the aggregate pdf through the product $\bar{\kappa} f_n$ and the refractive index m through the quotient $F(m)/E(m)$. Thus uncertainties in either the aggregate pdf or the refractive index propagate into the determination of the primary particle size d_{po} yielded by Eq. 22.

The data reduction proceeds as described below using the optical observations and TEM data reported in Table 2. The values of $\overline{R_g^2}$ are first found using Eq. 9 or 10 with an estimated value of D_f. The values of the primary particle diameters d_{pl} determined from the TEM observations [12] are used with $\overline{R_g^2}$ to find $\overline{n_1}$ from Eq. A2 with estimated values of $\bar{\kappa}$ and f_n (see below), $g(k\overline{R_g^2})$ from Eq. 16, ρ_{sa} from Eq. 13, K_{abs} from ρ_{sa} and the measured K_{ext}, and D_{30} from Eq. 20. The quantity $\overline{I^A(\theta_i)}/\overline{n^2}$ is then calculated and, when $q^2\overline{R_g^2} > 1.5D_f$, is used to determine the value of the fractal dimension D_f and the full calculation is reiterated. Finally the values of the number concentration of aggregates N_a and the optically determined primary particle size d_{po} are found.

In these experiments, individual measurements for light scattering and extinction were averaged in over 100 observations. For the scattering measurements (Q_{vv}) at heights z of 15, 20, and 70 mm, fluctuations owing to noise on the signal amounted to a probable error of $\pm 10\%$, which we estimated to be the uncertainty of these quantities. At intermediate heights (z = 30, 50, and 60 mm), the observed noise amounted to $\pm 2\%$. On the other hand, the observations at the lowest measured height (z = 10 mm) displayed $\pm 20\%$ fluctuations. Similar analysis for the extinction measurements yielded an estimated noise error of $\pm 1\%$. However, based on experience with repeated extinction measurements, the local extinction values are estimated to have an error of $\pm 10\%$. This error is largely due to slight asymmetries in the radial extinction profiles which are reflected in the subsequent tomographic inversion analysis.

Based on these considerations, the probable uncertainty in f_v at intermediate heights is estimated as $\pm 15\%$. The quantities R_g and D_{30} are believed to have similar uncertainties. In our procedure, TEM data on d_p is used for which small uncertainties are achieved ($\pm 10\%$). The quantities N_a, S_t, and $\overline{n^1}$ have the greatest uncertainty ($\pm 50\%$) that is aggravated in the case of the lowest height. The information conveyed in the figures given below should be viewed with this discussion in mind.

Uncertainties are also present in this calculation relating to the refractive index and the aggregate size pdf, which, in the data reduction procedure is characterized by the product $f_n\bar{\kappa}$. In the present calculation we use trial values of $f_n\bar{\kappa}$ to find the best agreement between the values of d_{po} yielded by Eq. 22 and the values d_{pl} yielded by TEM observations. As an objective procedure, we select the value of $f_n\bar{\kappa} = (f_n\bar{\kappa})_{min}$ that yields the smallest fractional rms value of $[d_{po} - d_{pl}]$ summed over all values of z for a given refractive index.

The three values of refractive index, which span the range of the numerous values applicable to soot that are quoted in the literature, have been employed in reducing the data and are listed in Table 3 along with the corresponding values of $(f_n\bar{\kappa})_{min}$. Of the several results given in Table 3, the value of $m = 1.90 - i0.55$ provides the most reasonable values of $f_n\bar{\kappa} = 5.5$ and for the aggregation rate K_a, as discussed below. This value of $f_n\bar{\kappa}$ corresponds to aggregate pdfs of intermediate widths, as described in the Appendix. (In estimating $\bar{\kappa}$ and thus $f_n\bar{\kappa}$ we employ a prefactor k_f appearing in the fractal power law equal to 9.0 that is based on experimental observations for soot particles; see the Appendix).

TABLE 2

Optical Observations and Other Input Data on the Laminar, Nonsmoking Ethene Flame (3.85 cm²/s)

Z (mm)	t^a (ms)	K_{ext} (cm^{-1})	$Q_{vv}(\theta_2)$ (cm^{-1} sr^{-1})	R_{12}	R_{13}	d_{pl}^b (nm)
10.	25.1	0.0657	4.68E-5	1.109	1.150	13
15.	31.3	0.235	1.58E-3	1.250	1.432	22
20.	36.1	0.443	5.47E-3	1.658	2.225	27
30.	44.1	0.836	1.54E-2	2.138	3.380	32
50.	56.4	0.828	1.38E-2	2.883	4.237	32
60.	61.4	0.459	6.21E-3	2.677	4.255	27
70.	66.5	0.0781	6.41E-4	2.037	2.402	19

[a] Derived from laser doppler anemometry observations [11].

[b] From thermophoretic sampling and TEM observations [12].

TABLE 3

Values of $(f_n\bar{\kappa})_{min}$ and K_a for Selected Values of Refractive Index

m	Ref.	$F(m)/E(m)$	$(f_n\bar{\kappa})_{min}$	$K_a(cm^3/s)$
$1.57 - i0.56$	Dalzell and Sarofim [13]	0.837	10.1	236×10^{-10}
$1.90 - i0.55$	Lee and Tien [14]	1.55	5.50	95×10^{-10}
$2.10 - i0.55$	Vaglieco et al. [15]	2.16	3.92	57×10^{-10}

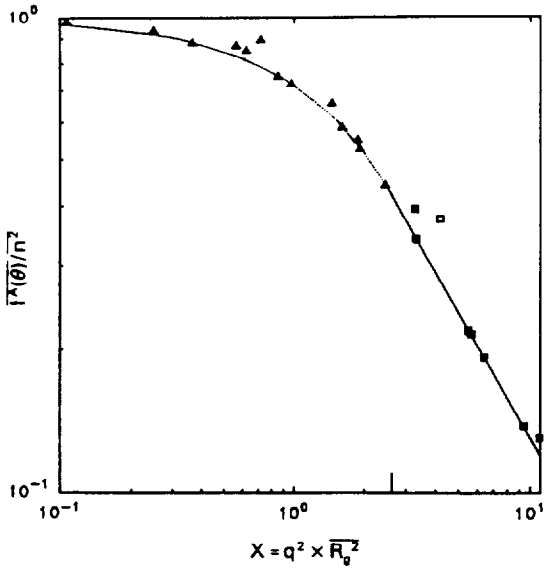

Fig. 1. Normalized intensity $\overline{I^A(\theta)}/\overline{n^2}$ versus $q^2\overline{R_g^2}$. The slope of the regression line for $q^2\overline{R_g^2} > 1.5D_f$ (solid squares) yields D_f of 1.74. See discussion in text.

DISCUSSION OF RESULTS

The graph of $\overline{I^A(\theta_i)}/\overline{n^2}$ versus x_i is shown in Fig. 1 using the observed volumetric cross sections and reduced values of N_a, d_{pl}, $\overline{n^1}$, and $\overline{R_g^2}$ to find the ordinate and the abscissa. The seven data points (solid squares) to the right in Fig. 1 lie in the power law regime where Eq. 8 is applicable. [One point, an open square, at the top of the flame where rapid burnout is in progress correlated poorly and was not used in the determination of D_f.] The slope of the least square straight line through these points yields a fractal dimension of 1.74. The smooth curve in Fig. 1 is the theoretical curve for the dimensionless cross section given by Eqs. 7 and 8 for a fractal dimension $D_f = 1.74$. The curvature of a mean line through the data points corresponds well to that of the theoretical curve, and the experimental points show the transition from Rayleigh scattering ($x \ll 1$), to Guinier regime ($x \approx 1$), and to the power law regimes.

The value $D_f = 1.74$ is in general agreement with the results of several experimental observations of soot aggregates in flames that fall within the range of 1.5–1.8 (see Table 4). These results are generally only slightly lower than the values, 1.7–1.9, that typically are found in numerous computer simulations of free molecular (ballistic) CCA. Noteworthy is the fact that the fractal dimension of the aggregation process in the flame, where primary particle growth and contraction occur successively, agrees with the computer simulations that use a constant primary particle diameter. This suggests, if only preliminarily, that the growth and oxidation processes do not significantly alter the fractal dimension of the aggregates formed in their presence.

The quantities f_v, d_{pl}, and D_{30} are plotted versus time in Fig. 2. These three curves show maximum values at about 56 ms, which corresponds to a height $z = 50$ mm. This point in the flame marks the transition from the growth region, where surface growth and CCA are cooperative, to the oxidation region where oxidation reactions oppose surface growth.

In Fig. 3 the number concentrations of the aggregates and primary particles N_a and N_p are plotted versus time. These values are consistent with the sustained action of CCA tending to increase aggregate size throughout the growth region and even into the oxidation region. The number concentration of the primary particles remains constant except at early and late times. The gas temperature and density remain essentially constant along the particle path of maximum soot concentration which, in the lower portion of the flame, lies within the high temperature flame front. The early time behavior is consistent with the possibility that some coagulation occurs at the beginning

TABLE 4

Summary of Experimental Determination of D_f for Soot Aggregates in Flames by Various Investigators

Investigators	Fuel and Flame Type	Method	D_f
Sampson, et al. [16]	C_2H_2 Diffusion Flame (Sample from smoke plume above flame)	TEM Observation	1.5 to 1.6
Zhang et al. [17]	CH_4/O_2 Premixed (Sample extracted to Optical cell)	Light Scattering, TEM	1.61 ± 0.06, 1.72 ± 0.10
Megaridis and Dobbins [3]	C_2H_4 Diffusion Flame	TEM Observation	1.62 ± 0.04 1.74 ± 0.06
Gangopadhyay et al. [18]	CH_4/O_2 Premixed Flame	In Situ Light Scattering	1.6 to 1.8
Charalampopoulos and Chang [19]	C_3H_8/O_2 Premixed	In Situ Light Scattering	1.7 ± 0.08
Sorensen et al. [20]	CH_4/O_2 Premixed	In Situ Light Scattering	1.70 to 1.75
Present study	C_2H_4 Diffusion Flame	In Situ Light Scattering with TEM	1.74 ± 0.1

of the region where surface growth is prominent.

The particle surface area and specific growth/oxidation rate are presented in Fig. 4. The latter is given by

$$f = \pm \frac{1}{S_t}\frac{dc_m}{dt} = \pm \frac{\rho_p}{S_t}\frac{df_v}{dt}, \tag{23}$$

where c_m is the particle mass per unit volume, S_t is the particle surface per unit volume, and ρ_p is the particle material density, which is taken to be 1.86 g/cm^3. The plus sign refers to the specific growth rate and the minus sign to the specific oxidation rate. The derivative in Eq. 23 was evaluated by differentiating a least-squares-fit to a third order polynomial.

The maximum specific growth rate shown in Fig. 4, 15×10^{-5} g/cm^2/s, is somewhat higher than previously reported for this flame [12] using a less detailed data reduction. This value is close to the maximum value reported for a premixed ethene flame [21]. The growth rate of the primary particles decreases as oxidation becomes dominant above the midflame height. The oxidation rate rises very rapidly as the aggregates approach the high-temperature envelope, which surrounds the soot-bearing luminous region and which is rich in the oxidizing OH and O_2 species. The oxidation rate

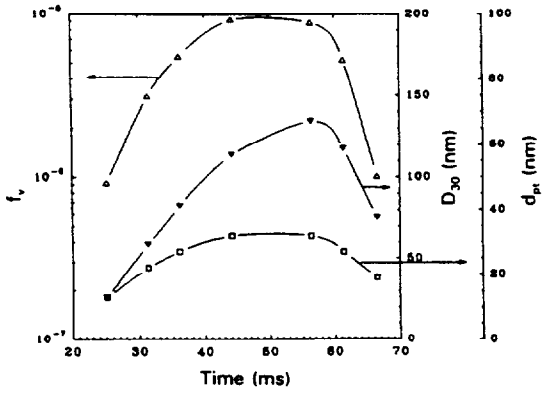

Fig. 2. Volume fraction f_v, primary particle diameter (from TEM) d_{pt}, and volume mean diameter D_{30} versus time.

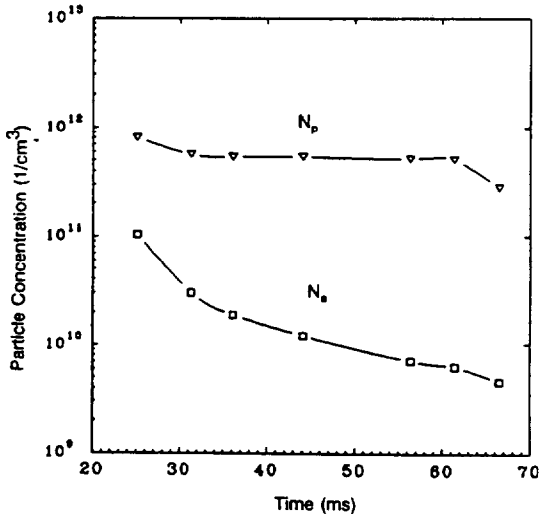

Fig. 3. Number concentration of primary particles N_p and of aggregates N_a versus time.

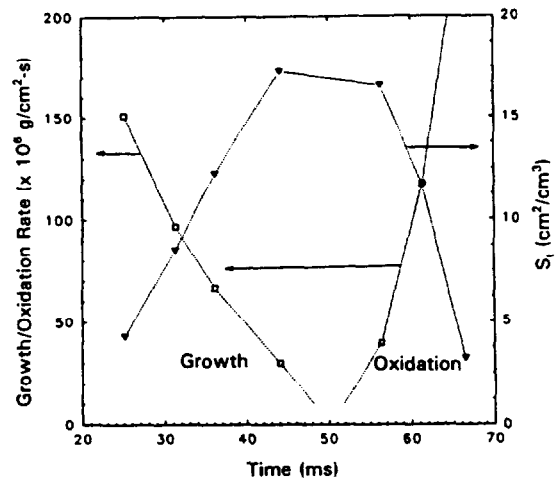

Fig. 4. Growth/oxidation rates, f, and surface area, S_t, versus time.

continues beyond 7.5×10^{-4} g/cm^2/s, which is measured at $z = 70$ mm. The specific oxidation rate that is reported for a methane diffusion flame ranges up to about 10^{-3} g/cm^2/s [22].

Figure 5 is a graph of the mean-square radius of gyration $\overline{R_g^2}$, the primary particle diameter as determined by TEM d_{pl}, and the average number of primary particles per aggregate $\overline{n^1}$. Both $\overline{R_g^2}$ and $\overline{n^1}$ reach peak values later than d_{pl} apparently because cluster–cluster aggregation continues in progress after oxidation of the primary particles commences. High-resolution probing of the soot burnout region of the flame would be required to determine if

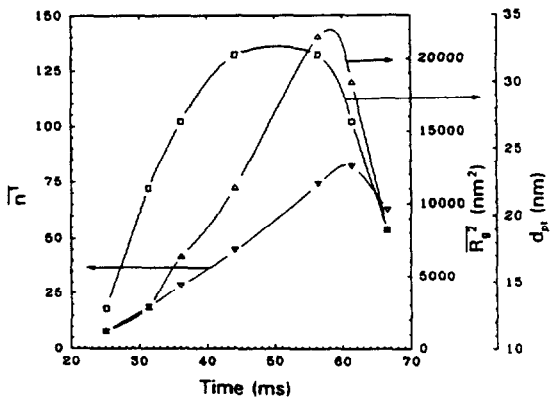

Fig. 5. Mean-square radius of gyration $\overline{R_g^2}$, average number of primary particles per aggregate $\overline{n^1}$, and primary particle diameter from TEM d_{pl} versus time.

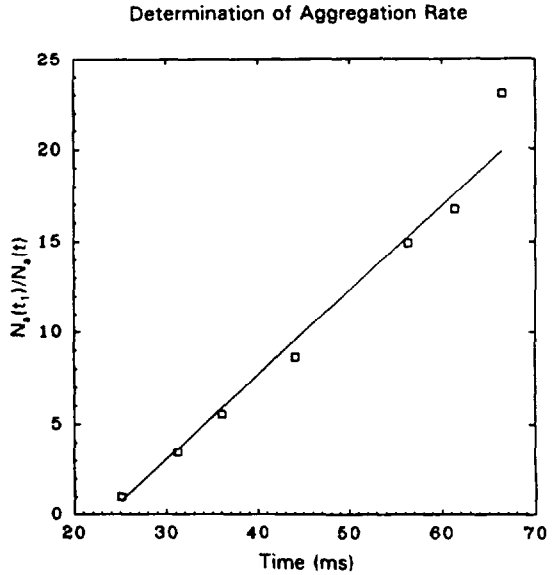

Fig. 6. $N_a(t_1)/N_a(t)$ versus time. The slope of the least-square straight line yields the cluster–cluster aggregation rate equal to 95×10^{-10} cm^3/s.

these maxima are an indication of aggregate breakup as a result of oxidation.

The disappearance of aggregates occurs through CCA and the aggregation rate is yielded by the first moment of the aerosol dynamic equation in the absence of particle generation. Provided the particle collision rate is not strongly size dependent, the result is

$$\frac{dN_a}{dt} = -\frac{1}{2}K_a N_a^2. \tag{24}$$

This equation can be rearranged as

$$K_a = \frac{2}{N_a(t_1)}\frac{d}{dt}\left(\frac{N_a(t_1)}{N_a(t)}\right). \tag{25}$$

In Fig. 6 we present a graph of the ratio $N_a(t_1)/N_a(t)$, whose slope is the CCA aggregation rate which shows a linear behavior except at late times when aggregate burnout is in progress. From Fig. 6, which is based on $m = 1.90 - i0.55$, we find a CCA rate of 95×10^{-10} cm^3/s.

The theoretical coagulation rate K_a for spherical particles small compared with the

molecular mean free path is

$$K_a = \left(\frac{3}{4\pi}\right)^{1/6}\left(\frac{6k_BT}{\rho_p}\right)^{1/2}\left(v_1^{1/3} + v_2^{1/3}\right)^2 \times\left(\frac{1}{v_1} + \frac{1}{v_2}\right)^{1/2}, \quad (26)$$

where k_B is the Boltzman constant, ρ_p is the particle density, T is the gas temperature, and v_1 and v_2 are the particle volumes. For two colliding spheres of equal diameter D this equation reduces to

$$K_a = 4\left(\frac{6Dk_BT}{\rho_p}\right)^{1/2}. \quad (27)$$

For a size D of 100 nm when $T = 1700$ K we find a theoretical value of K_a equal to 110×10^{-10} cm^3/s. The use of twice the mean-square radius of gyration in lieu of the particle diameter does not significantly change this rate, which varies as the square root of the particle length scale. The agreement between the observed aggregation rate and the theoretical coagulation rate is reasonable.

COMPARISON WITH DATA REDUCTION BASED ON RAYLEIGH AND MIE THEORIES FOR SPHERES

The data reduction based on aggregate cross sections shows significant differences from those employing Mie and Rayleigh cross sections for spheres. The volume mean diameter that is yielded in the case of the Mie and Rayleigh data reduction shows a much more moderate increase in the growth region and a very modest decrease throughout the oxidation region even though soot volume fraction is found to decrease dramatically. In the Rayleigh sphere data reduction, the particle number concentration tends to increase slightly throughout the growth region where CCA actually would be expected to cause N_a to decrease. In the Mie data reduction, the volume mean diameter can be calculated by one of two methods—from scattering/extinction ratio or from dissymmetry measurements. Of these two methods, the latter gives a larger volume mean diameter and smaller surface area per unit volume, and these self-contradictory results immediately call into question the applicability of Mie theory. The particle number concentration obtained from the Mie data reduction using scattering/extinction cross sections is invariant along most of the streamline. This implies the absence of CCA or that CCA is offset by an increase in the aggregate population through inception. Additionally, the Mie data reduction using dissymmetry measurements gives a much lower number concentration which decreases monotonically. This analysis also seems unreasonable since it yields more than twice the theoretical aggregation rate. The peak soot volume fraction is about 30% higher for Rayleigh and about 15% lower for Mie sphere data reduction at the intermediate heights where the aggregates are largest. Thus, while the Rayleigh data reduction ignores any contribution of scattering to extinction, the Mie data reduction appears to overestimate this contribution compared to the aggregate data reduction. Finally, the Rayleigh data reduction predicts a surface area per unit volume that is lower than the prediction aggregate theory by a factor of about two. The Mie theory prediction of this quantity is lower by a factor of 3–6 depending on the method by which the volume mean diameter is employed. These predictions are considered unrealistic in view of the well documented aggregate structure of the particles in this flame.

SUMMARY

The data reduction of the soot particle field that is based on the presence of aggregate morphology presents an internally consistent picture of the development of the soot particle field in the laminar ethene flame. This is summarized in Fig. 7, where the regions within this flame corresponding to the various processes are depicted.

Low in the flame there is an annular region of particle inception where preparticle chemical reactions produce a high concentration of primary particles which solidify and collide to form young aggregates. Detailed observations within the inception region are difficult because

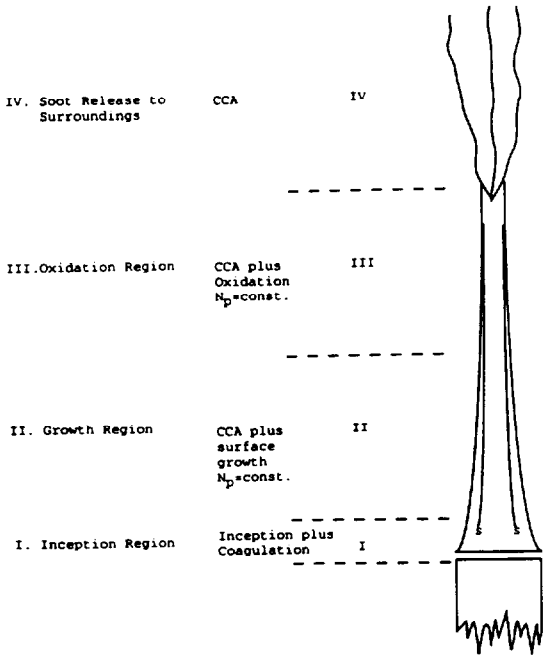

Fig. 7. A schematic representation of the soot aerosol dynamic processes in the laminar ethene diffusion flame.

of the rapid rates and high spatial gradients. The primary particle concentration that is established in the inception region remains unchanged along the soot particle path of maximum soot concentration throughout the flame until the particles are totally oxidized or, alternatively, released to the surroundings after partial oxidation.

Above the inception zone is the growth region where the primary particles grow from 10 to about 35 nm by surface growth, and CCA simultaneously causes cluster growth. The values of d_p, D_{30}, $\overline{R_g^2}$, and $\overline{n^1}$ increase while the primary particle concentration N_p remains constant.

The upper portion of the flame is an oxidation region wherein primary particles contract due to oxidation reactions. The size-related quantities d_p, D_{30}, and f_v decrease but again the primary particle number concentration remains relatively constant. Complete particle burnout occurs in this region in the case of the nonsmoking flame whose flame height is less than the smoke point height. Taller flames release smoke to the surroundings in the fourth region where chemical reactions cease to be important but CCA can continue to be present.

The aggregate data reduction of the scattering/ extinction measurements yields values of the fractal dimension that are in agreement with the value found by TEM for this same diffusion flame [3] as well as with in situ observations on various hydrocarbon flames (Table 4). The rate of aggregation of the clusters is found to be in general agreement with coagulation theory. The particle surface areas per unit volume are considered to be more reliably measured and these are expected to provide improved values of the soot specific growth and oxidation rates. Finally, only the aggregate data reduction yields a satisfactory description of the evolution of the soot aerosol and the regional partitioning of the soot aerosol dynamic processes within this flame.

This research was performed under the sponsorship of the U.S. Department of Commerce, National Institute of Standards and Technology, Center for Fire Research under grant number 60NANB01035 to the Pennsylvania State University and grant numbers 60NANB9D0975 and 60NANB1D1110 to Brown University. Two of the authors (RJS and TFR) would also like to acknowledge support by the Air Force Office of Scientific Research under Award No. AFOSR-87-0145. One author (RAD) was supported in part by the Army Research Office under Grant No. DAAL03-92-G-0023.

REFERENCES

1. Dobbins, R. A., Santoro, R. J., and Semerjian, H. G., *Twenty-Third Symposium (International) on Combustion*, The Combustion Institute, Pittsburgh, 1990, p. 1525.
2. Dobbins, R. A., and Megaridis, C. M., *Langmuir* 3:254–259 (1987).
3. Megaridis, C. M., and Dobbins, R. A., *Combust. Sci. Technol.* 71:95–109 (1990).
4. Schaefer, D. W., Martin, J. E., Wiltzius, P., and Cannel, D. S., *Phy. Rev. Lett.* 52:2371–2374 (1984).
5. Jullien, R., and Botet, R., *Aggregation and Fractal Aggregates*, World Scientific, Singapore, 1987, p. 46.
6. Botet, R., and Jullien, R., *Ann. Phys. Fr.* 13:153–221 (1988).
7. Dobbins, R. A., and Megaridis, C. M., *Appl. Optics* 30:4747–4754 (1991).
8. Semerjian, H. G., Santoro, R. J., Goulard, R., and Emmerman, P. J., in *Fluid Mechanics of Combustion Systems* (T. Morel, R. P. Lohmann, and J. M. Rackley,

Eds.), American Society of Mechanical Engineers, New York, 1981, p. 119.
9. Mountain, R. D., and Mulholland, G. W., *Langmuir* 4:1321–1326 (1988).
10. Santoro, R. J., Semerjian, H. G., and Dobbins, R. A., *Combust. Flame* 51:203–218 (1983).
11. Santoro, R. J., Yeh, T. T., Horvath, J. J., and Semerjian, H. G., *Combust. Sci. Technol.* 53:89–115 (1987).
12. Megaridis, C. M., and Dobbins, R. A., *Combust. Sci. Technol.* 66:1–16 (1989).
13. Dalzell, W. H., and Sarofim, A. F., *J. Heat Transf.* 91:100–104 (1969).
14. Lee, S. C., and Tien, C. L., *Eighteenth Symposium (International) on Combustion*, The Combustion Institute, Pittsburgh, 1981, p. 1159.
15. Vaglieco, B. M., Baretta, F., and D'Alessio, A., *Combust. Flame* 79:259–271 (1990).
16. Sampson, R. J., Mulholland, G. W., and Gentry, J. W., *Langmuir* 3:272–281 (1987).
17. Zhang, H. X., Sorensen, C. M., Ramer, E. R., Oliver, B. J., and Merklin, J. F., *Langmuir* 4:867–871 (1988).
18. Gangopadhyay, S., Elminyawi, I., and Sorensen, C. M., *Appl. Opt.* 30:4859–4864 (1991).
19. Charalampopoulos, T. T., and Chang, H., *Combust. Flame* 87:89–99 (1991).
20. Sorensen, C. M., Cai, J., and Lu, N., submitted.
21. Harris, S. J., *Combust. Sci. Technol.* 72:67–77 (1990).
22. Garo, A., Prado, G., and Lahaye, J., *Combust. Flame* 79:226–233 (1990).
23. Mulholland, G. W., Personal communication, 1991.

Received 30 March 1992; revised 18 September 1992

APPENDIX: THE MOMENT RATIOS $\bar{\kappa}$ AND f_n

The fractal power low relates the number of primary particles per aggregate to the ratio R_g/d_p:

$$n = k_f\left(\frac{R_g}{d_p}\right)^{D_f}, \tag{A1}$$

where D_f is the fractal dimension and k_f is the prefactor. The definition of the mean-square radius of gyration for a population of polydisperse aggregates consisting of monodisperse primary particles that is given by Eq. 6 is highly advantageous as discussed elsewhere [7]. The appropriate version of the power law expression that is applicable to a population of polydisperse aggregates is then found by solving Eq. A1 for R_g, substituting it into Eq. 6 and rearranging the result,

$$\overline{n^1} = \bar{\kappa}\frac{\overline{R_g^2}}{d_p^2}, \tag{A2}$$

where $\bar{\kappa}$ is defined by

$$\bar{\kappa} = \frac{k_f^{2/D_f}\Sigma p(n)n\Sigma p(n)n^2}{\Sigma n^{2/D_f}n^2p(n)}. \tag{A3}$$

When $D_f = 2.0$, $\bar{\kappa}$ is reduced to the quotient of k_f and a high moment ratio of the aggregate pdf:

$$\bar{\kappa} = k_f\Big/\left(\frac{\overline{n^3}}{\overline{n^2}\,\overline{n^1}}\right). \tag{A4}$$

The polydispersion power law, Eq. A2, and thus also $\bar{\kappa}$ enter into the expressions for the differential and total scattering cross sections when they are expressed in terms of the mean-square radius of gyration.

While there is now a well documented literature on the value of the D_f from both experimental observations and from computer simulations of cluster–cluster aggregation, very limited information exists on the value of k_f and thus also on $\bar{\kappa}$. In a previous work [1] the value of $k_f = 5.8$ that originates from a computer simulation [9] was employed. We now seek to determine an experimental value of k_f for use in determining $\bar{\kappa}$.

The first source of data on k_f is provided by the 36 aggregate subset sample of soot particles originating from an acetylene diffusion flame [16, 23]. These investigators reported n and R_g as determined from the two-dimensional projection, and also the maximum dimension of the aggregate L_{mx}. From these data we find the average value of the ratio of L_{mx}/R_g to be 3.55. Also from the tabular data of n and R_g listed in the same work, we directly find $k_f = 9.22$ and $D_f = 1.40$ by a regression analysis. The latter low value of D_f perhaps results from the small size of this subset sample. This body of data suggests a higher value of k_f for soot aggregates than was obtained from the computer simulation.

A second source of data on k_f is found using the above experimentally derived average value of L_{mx}/R_g to convert the observed L_{mx} [3] for the experimental data reported on the nonsmoking ethene flame. This leads to values of $k_f = 8.9$ and 8.3 for the two aggregate populations that were analyzed. Based on all of above information, we adopt a value of $k_f = 9.0$ as an experimentally based value that is specifically applicable to soot aggregates.

Values of $\bar{\kappa}$ are found from its definition Eq. A3 using the detailed statistics of the latter two applicable population data sets. The resulting values are found to be $\bar{\kappa} = 2.89$ and 2.60 corresponding to aggregate pdfs of intermediate width.

The moment ratio f_n given by Eq. 4 is more readily determined from the above sources of data to lie within the range of 1.6–1.8. This value is only somewhat smaller than the value applicable for the continuous self-preserving particle size distribution function for coagulating spherical droplets. Because f_n is defined in terms of low moments of the aggregate pdf, its value is more narrowly circumscribed and, accordingly, the value of $f_n = 1.70$ is considered to be reliable for intermediate pdf widths.

The influence of the width of the aggregate population can be investigated by adopting a particular function for the pdf. The discrete log normal distribution is

$$p(n) = \frac{\exp\left[-\left(\frac{\ln \frac{n}{n_g}}{3\sqrt{2}\,\sigma_g}\right)^2\right]}{3\sqrt{2\pi}\,\sigma_g s_0 n} \qquad \text{(A5)}$$

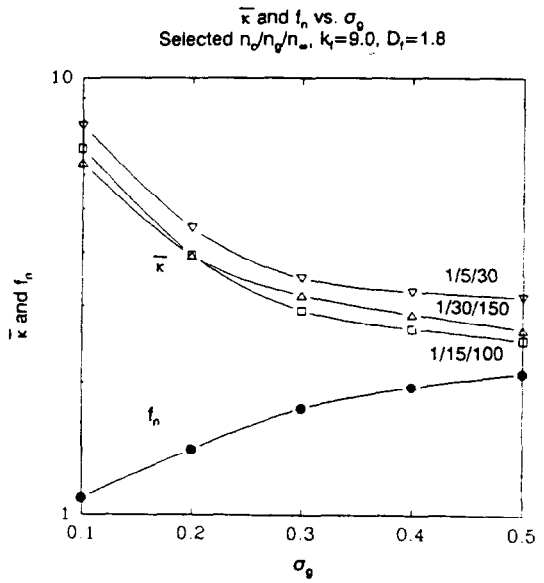

Fig. A1. $\bar{\kappa}$ and f_n versus σ_g as calculated from a discrete log normal distribution for selected values of $n_0/n_g/n_x$.

where σ_g is the geometric standard deviation, n_g is the geometric mean number of primary particles per aggregate, and s_0 is a constant defined such that $p(n)$ summed over all sizes (n_0 to n_x) is unity. Values of f_n and $\bar{\kappa}$ for log normal distributions can be found by inserting Eq. A5 into Eqs. 4 and A3 and evaluating the indicated summations for particular values of n_0, n_g, n_x, σ_g, D_f, and k_f. Some results are presented in Fig. A1 for $D_f = 1.80$ and $k_f = 9.0$, and with $n_0/n_g/n_x$ estimated to bracket the range of interest. For $\sigma_g = 0.300$ corresponding to a moderate width of the pdf, the value of $\bar{\kappa}$ ranges from 2.9 to 3.5 and f_n ranges from 1.63 to 1.75. Reasonable values of $f_n\bar{\kappa}$ are 5.1 to 5.9 for aggregate populations of intermediate width.